# Optical Thickness Measurements of Vacuum Ultraviolet Radiation in the X2 Expansion Tube

Umar A. Sheikh [1], Richard G. Morgan [2] and Timothy J. McIntyre [3]
*The University of Queensland, QLD, 4072*

**Experiments were conducted in the X2 expansion tube to measure vacuum ultraviolet radiation from shock layers representative of re-entry conditions at flight equivalent velocities of 10.0 km/s and 12.2 km/s. Cylindrical models of varying lengths were used to make measurements of different depths of radiating gases. Spectral emission measurements were made, imaging parallel to the surface of the models along the stagnation streamline. Ratios of integrated spectral bands were compared to quantify increases in radiance with increasing depth of radiating gas. Significant increases in observed radiance were measured with increasing model length. Comparisons were made with simulations that assumed an optically thin shock layer and it was found that over 98.9% of the total vacuum ultraviolet radiation emitted was self-absorbed. Good agreement was found between the simulations and measurements of total radiance for the different depths of radiating gas. These results highlight the need to accurately quantify the opacity of a shock layer and spectral line broadening as it significantly increases the radiance emitted from the shock layer in the vacuum ultraviolet region.**

---

[1] Post-Doctoral Research Fellow, The Centre for Hypersonics, School of Mechanical and Mining Engineering, The University of Queensland, now at the Swiss Plasma Center, Ecole Polytechnique Federal de Lausanne, Switzerland umar.sheikh@epfl.ch
[2] Director of the Centre for Hypersonics, School of Mechanical and Mining Engineering, The University of Queensland, r.morgan@uq.edu.au
[3] Associate Professor, School of Mathematics and Physics, The University of Queensland, t.mcintyre@uq.edu.au

## I. Introduction

Modelling convective and radiative heat transfer to the surface of a re-entry vehicle is a difficult undertaking for design engineers. Convective heating can be readily studied at temperatures much lower than those of radiating shock layers and is therefore relatively well understood, leading to small design safety factors. Conversely, radiative heating is a phenomenon that is of significance at high temperatures and increases significantly with temperature. This makes the study of radiative heat transfer a much greater challenge and results in larger uncertainties in the prediction of radiative heat loads, which in turn lead to large safety factors in the design of thermal protection systems[1]. At certain high heat flux points on a superorbital re-entry trajectory, over 40% of the total radiative heat flux can originate in the vacuum ultraviolet (VUV) region between 100 nm and 200 nm[2]. Due to complex physical phenomena such as optical thickness or opacity, spectral line broadening and the difficulties associated in measuring VUV radiation, this region is not well understood and is responsible for the bulk of the uncertainties associated with calculating radiative heat flux.

A gas is considered to be optically thin when it is transparent to photons, leading to a linear increase in spectral radiance with respect to depth of the radiating gas. As a gas begins to absorb photons and scatter light, the transmissivity drops and the gas is described as optically thick. For an optically thick gas, the relationship between spectral radiance and depth of radiating gas is no longer linear because a fraction of the photons emitted by the gas are reabsorbed before they can escape. Therefore, for an optically thick gas, the transmissivity of the gas is a critical factor in calculating the spectral radiance. The transmissivity ($\tau$) of a gas is a function of the number density of the attenuating species ($N$), with an absorption coefficient ($\sigma$) and path length ($l$) through the absorbing gas, as described by the Beer-Lambert law, given in Equation 1.

$$\tau = exp(-\sigma l N) \tag{1}$$

Provided the gas is in thermodynamic equilibrium, its transmissivity will asymptote towards zero as it approaches the black-body limit for a given temperature and wavelength. At temperatures representative of shock layers during re-entry, the black-body limit in the VUV spectral range is relatively low compared with the UV and visible parts of the spectrum. Coupled with the fact that

transitions in the VUV are high energy and the emission cross-sections are orders of magnitude higher than in the UV and visible regions, a significant portion of the emitted VUV radiation is self-absorbed. Previous studies have shown that over 99% of the VUV emission for some spectral lines is self-absorbed in the shock layer, yet the small fraction that reaches the surface is responsible for over 40% of the total radiative heat flux [2]. The large radiative heat flux observed for such an optically opaque spectral region is to a large extent due to the radiance emitted across the broadened line profile of the transition.

Physical processes such as Doppler broadening and pressure broadening smear the wavelength range over which each transition emits photons. Likewise, the absorption coefficient also varies either side of the nominal wavelength of a given transition. As the number of radiating particles is increased in the line of sight, the physical width of the spectral line will become larger. The imposed black-body limit on the VUV spectral range causes the spectral lines to be saturated, however, with an increasing number of particles in the path length, the spectral emission further from the nominal wavelength continues to increase. This effect is shown in Figure 1 for a series of increasing depths of radiating flow field. This process clearly shows that spectral line broadening in the VUV spectral range can be a significant contributor to the integrated heat flux incident on a re-entry craft and must be accurately accounted for.

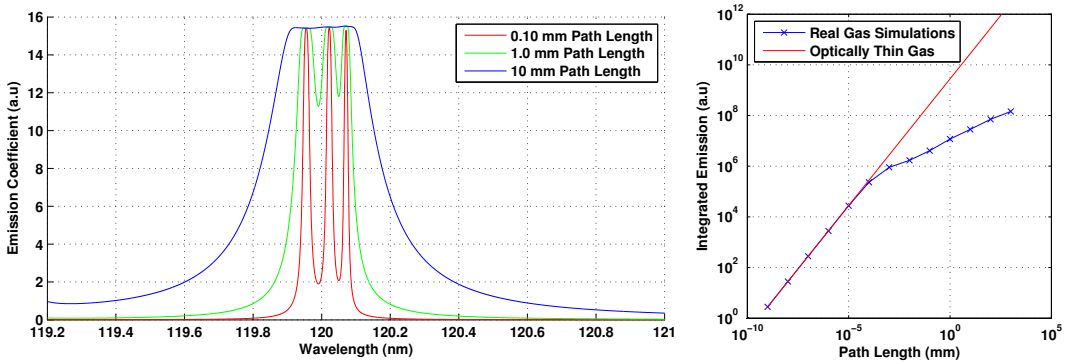


**Fig. 1 Calculated spectra for atomic nitrogen in thermochemical equilibrium at 7,000 K and atmospheric pressure through varying depths of radiating flow fields. Computations carried out using the Specair program[3].**

VUV spectral measurements relevant to re-entry conditions at high heat flux have been previ-

ously conducted at four facilities, not including the one used in this study[4]. These facilities are the EM2C plasma torch[5], the PWK plasma wind tunnel at IRS[6] and the EAST and HVST shock tubes at NASA and JAXA[7, 8]. The only facility in this group that has measured VUV radiation through varying optical path lengths is the EM2C plasma torch. However these measurements were only carried out for wavelengths above 170 nm and therefore did not cover the bulk of the VUV spectral range[9]. Consequently, the only facility currently capable of producing VUV spectral measurements through varying optical path lengths is the X2 expansion tube facility. This is achieved in the X2 expansion tube by varying the size of the models used to produce different lengths of radiating gases. Measurements through varying optical path lengths allow direct investigation of radiative transport through a shock layer, the opacity of spectral regions in the VUV and the quantification of increases in integrated spectral emission with increasing depth of radiating flow field.

## II. Facility Description

The X2 expansion tube at The University of Queensland is a free piston, compressed gas driven expansion tube capable of producing flows with enthalpies in excess of 175 MJ/kg for test times in excess of 150 $\mu$s. For this study, the expansion tube was operated with a single driver tube and a 208 mm diameter nozzle configuration as shown in Figure 2. The diaphragm materials used were carbon steel for the primary diaphragm and aluminium for the secondary diaphragm. A full description of the facility is available in Gildfind et al. [10].

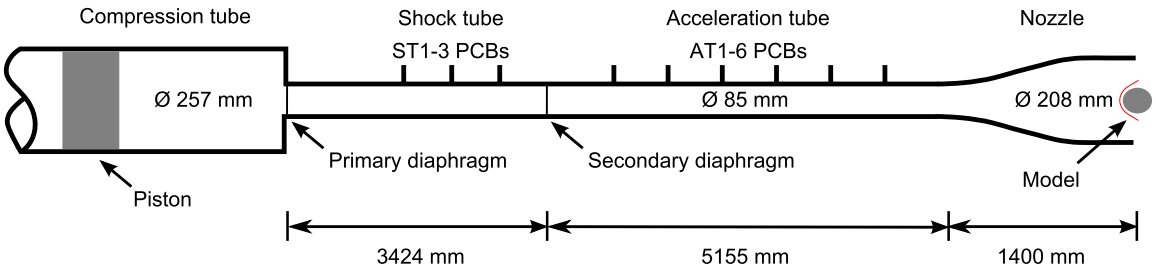


**Fig. 2 Schematic of the X2 expansion tube configuration used for this study. ST1-3 and AT1-6 PCBs are shock tube (ST) and acceleration tube (AT) pressure transducers used to measure static pressure and infer shock speeds.**

### A. Operating Conditions

Two conditions were utilized for this study matching 10.0 km/s and 12.2 km/s flight equivalent enthalpies. Previous shot data and basic shock wave relations, as outlined in Gildfind [11], were utilized to compute the fill pressures required. These estimates were tested experimentally using pressure transducers to measure static pressure and shock velocity, and pitot probes to measure the produced flow. The measured values were used in conjunction with the numerical codes *Pitot* [12] and CEA [13] to calculate the flow conditions, assuming equilibrium chemistry at the nozzle exit. Full condition development details are available in Sheikh 2014 [9] and the free stream properties of the test gas are presented in Table 1.

**Table 1 Free stream test conditions calculated using *Pitot* and available measured values.**

| **Condition 1** | | |
|---|---|---|
| Parameter | Calculated | Measured |
| Primary shock velocity (km/s) | 4.76 | 4.70 ±0.12 |
| Secondary shock velocity (km/s) | 9.57 | 9.60 ±0.30 |
| Static pressure at nozzle entry (Pa) | 4,710 | 5,000 ±750 |
| Pitot pressure (kPa) | 115 | 115 ±12 |
| Test gas velocity (km/s) | 9.71 | N/A |
| Test gas temperature (K) | 2,500 | N/A |
| Test gas Mach number | 10.6 | N/A |
| Test gas density (kg/$m^3$) | $1.26\times10^{-3}$ | N/A |
| Test gas enthalpy (MJ/kg) | 50.3 | N/A |
| Test gas static pressure (Pa) | 930 | N/A |
| **Condition 2** | | |
| Parameter | Calculated | Measured |
| Primary shock velocity (km/s) | 5.64 | 5.70 ±0.15 |
| Secondary shock velocity (km/s) | 11.7 | 11.50 ±0.40 |
| Static pressure at nozzle entry (Pa) | 4,460 | 7,000 ±1800 |
| Pitot pressure (kPa) | 135 | 140 ±28 |
| Test gas velocity (km/s) | 11.8 | N/A |
| Test gas temperature (K) | 2,800 | N/A |
| Test gas Mach number | 11.9 | N/A |
| Test gas density (kg/$m^3$) | $1.00\times10^{-3}$ | N/A |
| Test gas enthalpy (MJ/kg) | 74.5 | N/A |
| Test gas static pressure (Pa) | 870 | N/A |

## III. Experiment Design

The shock layer formed around a model is comprised of three-dimensional non-uniform flow at either edge and a uniformly radiating mid-section. Variation in the length of the model maintains the same non-uniform flow at either edge whilst altering the length of the uniformly radiating mid-section. The models used in these experiments were 25 mm tall with a front-face radius of curvature of 19 mm. Three model lengths of 20 mm, 45 mm and 90 mm were used. The model shapes and a depiction of the experiment concept are presented in Figure 3.

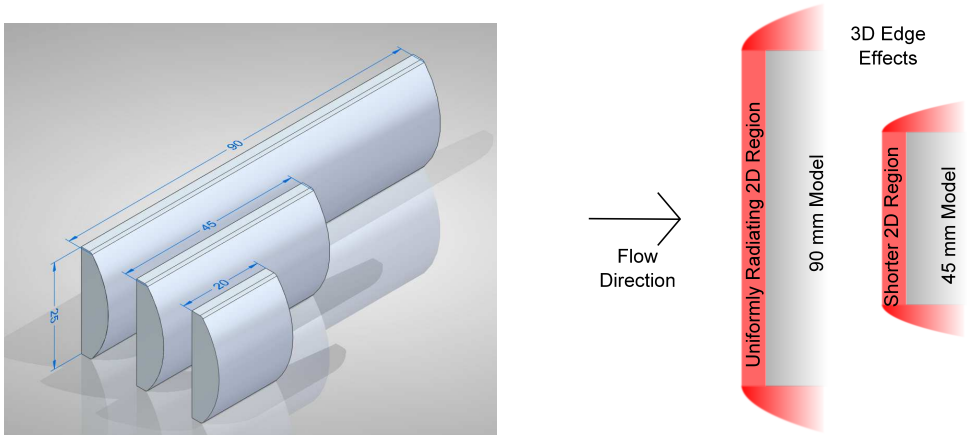


**Fig. 3 Left - Depiction of model shapes and lengths used. Right - Self absorption experiment concept showing the top down view of varying length models used to change the depth of a uniformly radiating two-dimensional region.**

### A. Emission Spectroscopy System

Spectral measurements were made imaging the shock layer across the surface of the model using an optical system composed of a flat mirror and a focussing mirror with a focal length of 500 mm. Both mirrors were coated with an Acton Optics #1200 coating for optimal performance across the wavelength range of interest. The spatial axis of the spectroscopy system was aligned with the stagnation streamline of model, as shown in Figure 4. The optical focussing system was designed to have a magnification of 0.85 resulting in the ability to spatially measure across 7.8 mm, ensuring the entire shock layer was imaged. A limiting aperture of 10.0 mm was placed on a focussing mirror to ensure the depth of field covered the entire 90 mm model with a circle of confusion of 0.35 mm.

The final details of the optical system designed are presented in Table 2

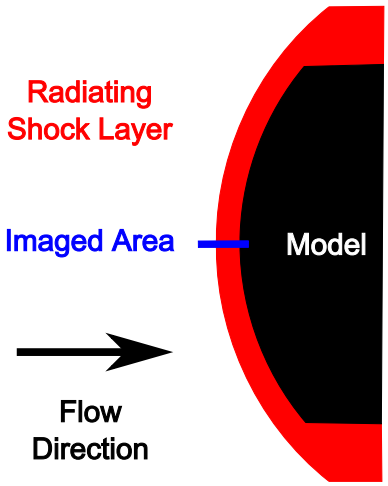


**Fig. 4 Alignment of spectrometer spatial axis with the stagnation streamline of the model.**

**Table 2 Details of the focussing optical system produced.**

| | |
|---|---|
| Focussing mirror to model centreline (mm) | 1088 ±1 |
| Focussing mirror to slit (mm) | 925 ±1 |
| Aperture (mm) | 10.0 ±0.3 |
| F-Number | 50.0 ±1.3 |
| Depth of field (mm) | 90 ±3 |
| Calculated circle of confusion (mm) | 0.35 |

VUV radiation is strongly absorbed by molecular oxygen and water vapour found in air and the free stream test gas produced by the expansion tube. Consequently, the optical path between the radiating shock layer and the detection device must be contained within a high vacuum environment. A high vacuum chamber was designed and constructed to house the focussing optics and a series of evacuated light tubes were employed to extend the high vacuum to within 10 mm of the radiating shock layer. The evacuated light path was sealed by a magnesium fluoride window mounted within a 'fence'. The role of the fence was to produce an acute angled shock wave that would dissociate the molecular oxygen in the core flow directly in front of the viewing window whilst ensuring the disruption was small enough not to affect the shock layer formed over the model. An annotated image of the set up during testing is shown in Figure 6. Based on the Lu et al. [14] absorption cross-sections for molecular oxygen, it was calculated that the absorption in the core flow between

the radiating shock layer and the window would be less than 2% due to the small size of the gap, relatively low pressure of the free stream flow and the partially dissociated state of oxygen within the test gas. This was experimentally verified by reducing the distance between the shock layer and the fence until there was no increase in signal strength measured, implying there was no further reduction in absorption of the signal by the coreflow[9].

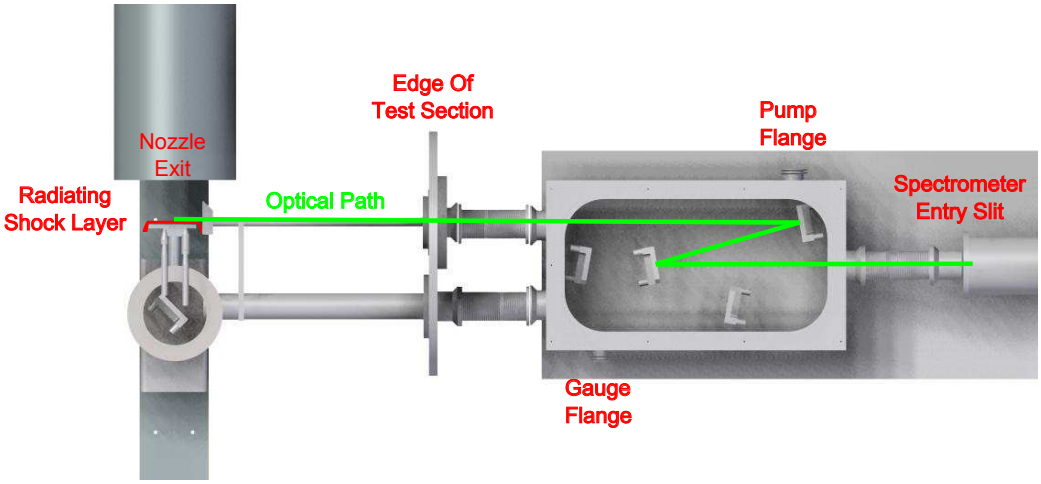


**Fig. 5 Imaging optics to observe radiation across the surface of the model and high vacuum optical path. Image drawn to scale.**

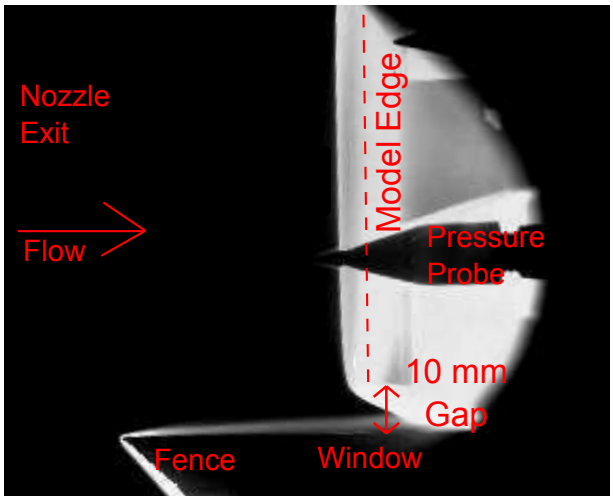


**Fig. 6 Top down view of fence and window position with a 10 mm gap to the blunt model.**

*1. Spectrometer*

A McPherson NOVA 225 1.0 m focal length, normal incidence spectrometer coupled to an Andor iStar generation 2 ICCD was the spectroscopy system used in this study. A 300 lines/mm grating was used to allow for a wavelength range of 115 nm to 175 nm in each image. There are 512 pixels in the spatial axis of the CCD and 2048 pixels in the spectral axis, providing a calculated spectral resolution of 0.06 nm/pixel. The slit width was set to 25 $\mu$m resulting in an instrument function of 0.20 nm half-width-full-maximum for the system, inferred from the 121.5 nm deuterium calibration lamp spectral line [4, 9].

*2. Calibration*

The emission spectroscopy system was calibrated using an in-situ calibration technique utilizing a deuterium calibration lamp. The deuterium lamp was calibrated at the Physikalisch-Technische Bundesanstalt [15] and is provided with a calibrated spectral radiance. An in-situ calibration approach was utilized as it accounts for any variation in alignment, aperture size, transmission and reflectance of optical elements from the given values as they are all in the optical path during calibration. The system sensitivity is presented in Figure 7 and was calculated using Equation 2:

$$\text{System sensitivity}(\lambda) = \frac{\text{ICCD counts}}{\text{Calibrated spectral lamp radiance}} \tag{2}$$

*3. Uncertainty Analysis*

The five terms most influential in calculating the level of uncertainty in emission spectroscopy are the radius of the aperture, distance to the aperture, the optical depth of the radiating gas, optical magnification and optical losses [16]. All optical aspects, including magnification of the optical system and capture solid angle, are accounted for in the in-situ calibration. The size of the models dictate the optical depth of the radiating gas and these are known accurately. The three-dimensional edge effects are not known accurately but are assumed to be constant between models. Consequently the emission spectroscopy system uncertainty is limited to the uncertainty of the calibration lamp itself and these values are outlined in Table 3.

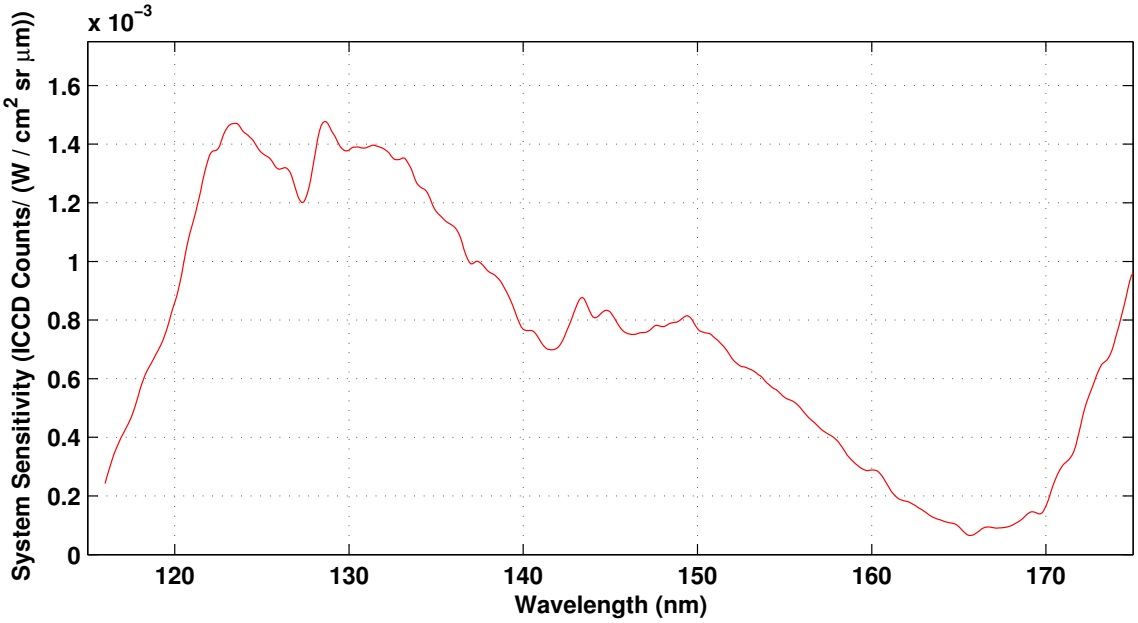


**Fig. 7 System sensitivity as a function of wavelength.**

**Table 3 Relative uncertainty of the calibration lamp [15].**

| Spectral Range (nm) | Spectral Bandwidth (nm) | Relative Expanded Uncertainty (k=2) |
|---|---|---|
| 116.0 - 120.4 | 0.8 | 14% |
| 120.6 - 122.6 | 0.8 | 36% |
| 122.8 - 170.0 | 0.8 | 14% |
| 172.0 - 410.0 | 1.6 | 7% |

## IV. Experimental Results

In each experiment a two-dimensional image is recorded consisting of a wavelength axis (horizontal) and a spatial axis (vertical). The wavelength is calibrated by recording an image from a spectral lamp and identifying known spectral features. The physical scale is determined from the measured magnification of the system. The orientation is such that flow along the stagnation streamline is imaged with the shock front near the top of the image and the body towards the bottom. A raw image captured during an experiment is shown in Figure 8.

Before an image is calibrated, a dark frame is subtracted to remove background noise. Stray light measurements were not possible during an experiment but were instead made using the calibration lamp as an in-situ source and stray light was found to be negligible. Conversion of measured

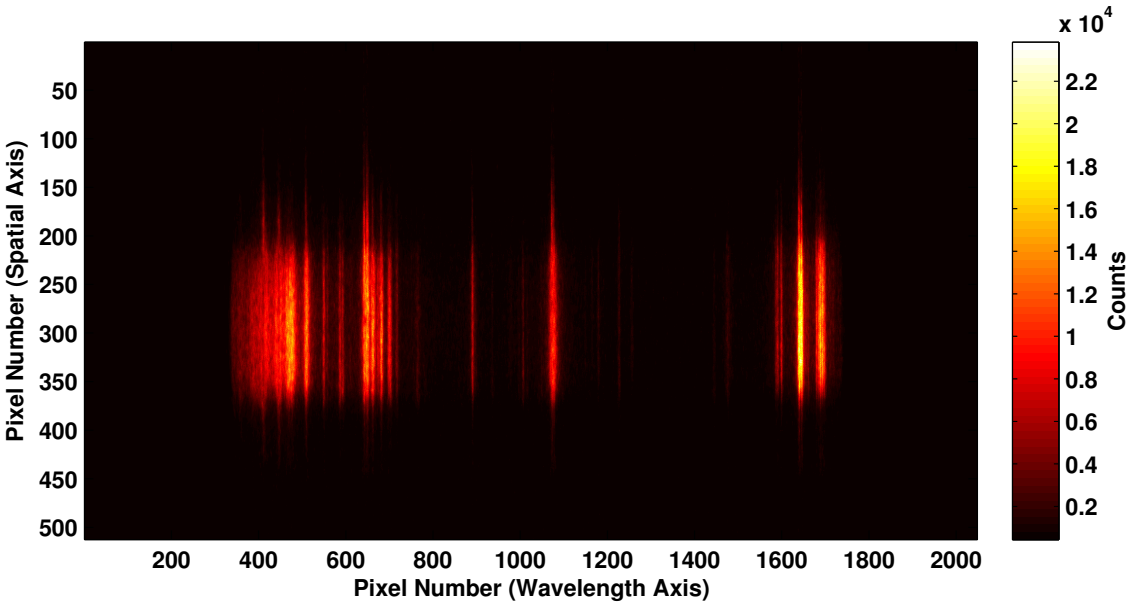


**Fig. 8 Raw image acquired on the ICCD observing across the surface of the model at Condition 2.**

counts to spectral radiance, as shown in 9a, is carried out using the approach outlined in Section III.A.2. Spectral integration of the recorded image allows for an intensity profile along the stagnation streamline to be calculated, as shown in Figure 9b. The initial rise in intensity depicts the shock front and this is not measured as an instantaneous increase in spectral intensity due to the inherent aberrations within the optical measurement system and finite flow length required to dissociate the gas and transfer energy into the appropriate temperature modes before the measured transitions can begin to radiate.

Figure 9c shows a spectrum of the flow. It is created by spatially averaging across the approximately constant emission region of the shock layer shown by the two red horizontal lines in Figure 9b. It shows a range of spectral features that can be used in detailed analysis of the shock layer.

### A. Spectral Line Identification

Each spectral line produced through radiative emission can be traced back to a single or closely spaced set of transitions. All spectral line peaks measured in the steady state emission region of the shock layer produced in this study are produced by atomic species, and can therefore can be identified using the National Institute of Standards and Technology [17] spectral line database. A

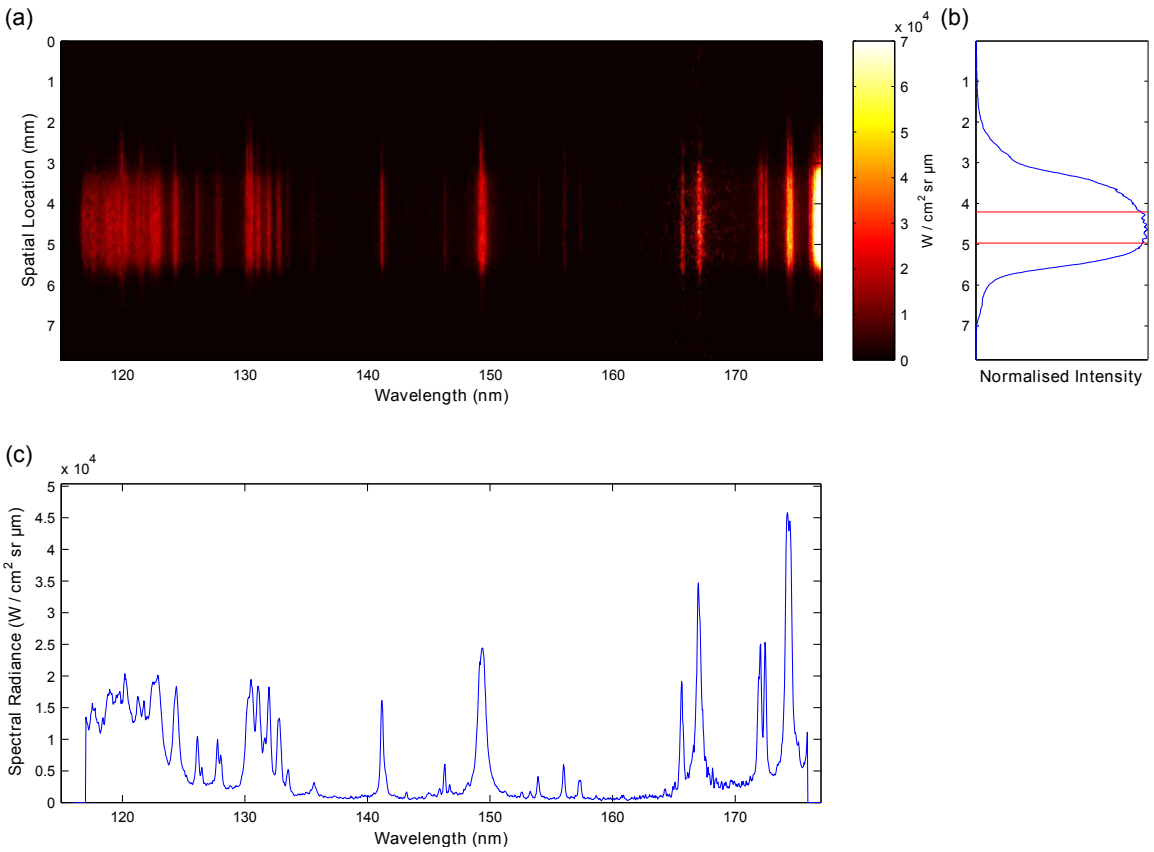


**Fig. 9 (a) - Calibrated image for the 90 mm model at Condition 2. (b) - Spectrally integrated profile showing the spatial distribution of the recorded image. The red lines indicate the spatial region termed the steady state emission region. (c) - Spectrum produced in the steady state emission region.**

sample spectrum with identified atomic species representing each spectral line is presented in Figure 10.

All carbon, iron, hydrogen and aluminium features are considered contaminants as they are produced by the operation of the expansion tube. Carbon and iron are believed to be entrained from the walls of the expansion tube and the surface of the model. Aluminium contamination occurs as a result of using aluminium sheet for the secondary diaphragm, which is positioned ahead of the test gas at the time of firing. Vaporised diaphragm material is able to accelerate at almost the same rate as the test gas and can enter the radiating shock layer during the test time. Hydrogen contamination is a result of water vapour out-gassing from the walls of the shock tube whilst it is at low pressures required for the operation of the expansion tube. All spectral lines produced by

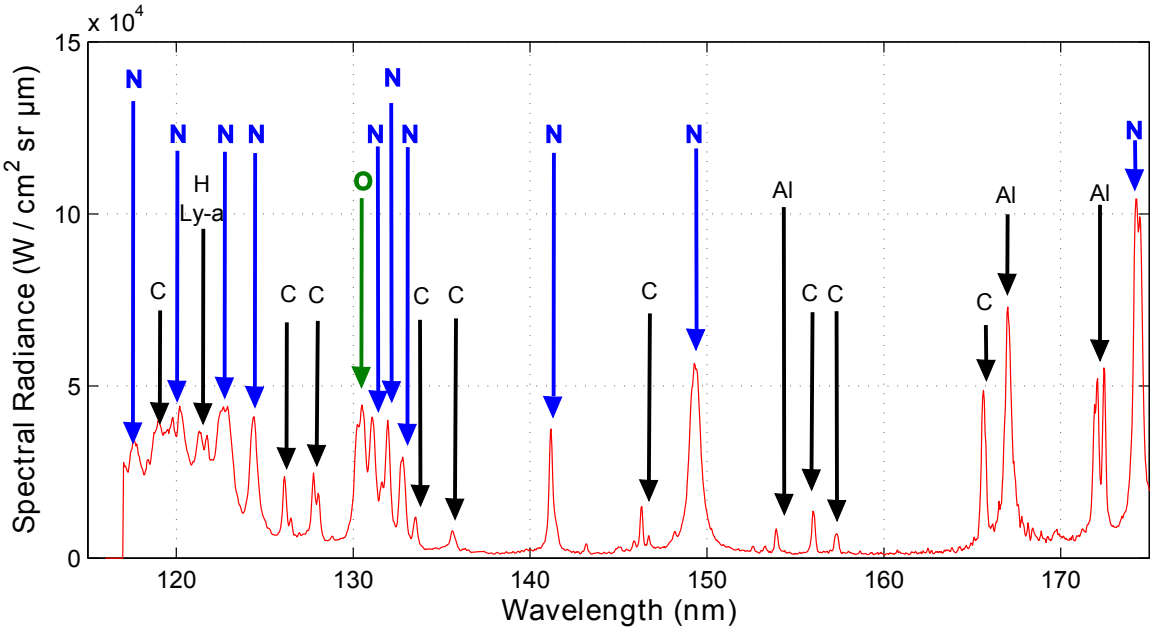


**Fig. 10 Chemical species responsible for each spectral line observed at Condition 2. [4]**

contaminant species are ignored in the analysis as the level of contamination between experiments may be variable.

### B. Datasets Produced

The spectra measured in the steady state emission region across the surface of each model are presented in Figures 11 and 12. Regions dominated by contaminants have been removed for this study. It is apparent that the intensities of the spectra measured do not scale with the varying depth of radiating flow field produced by each model. This lack of scaling is due to the optical opacity of the shock layer.

A secondary factor affecting the measured spectral line intensities is the finite resolution of the spectroscopy system, or the instrument function. This limitation stems from the finite physical size of the spectrometer slit, the dispersion of the grating, focus of the spectrometer and the resolution of the detector, leading to a wavelength range, rather than a given wavelength, to be integrated on each pixel. The resulting measured spectral line peak therefore consists of a combination of the peak spectral line emission, and a portion of the energy emitted either side of the nominal wavelength. The impact of the 0.2 nm half-width-full-maximum instrument function on each spectral line varies

depending on the level of physical broadening, which is unique for each spectral line, and this is further investigated in Section V.B.

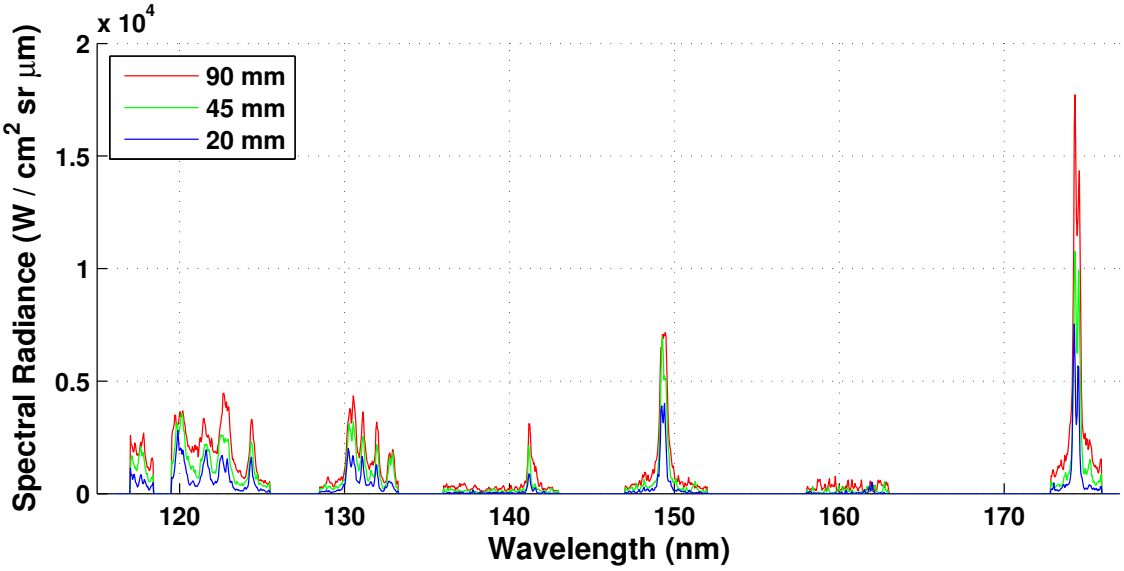


**Fig. 11 Comparison of spectra produced in the steady state emission region across models of lengths 90 mm, 45 mm and 20 mm at Condition 1.**

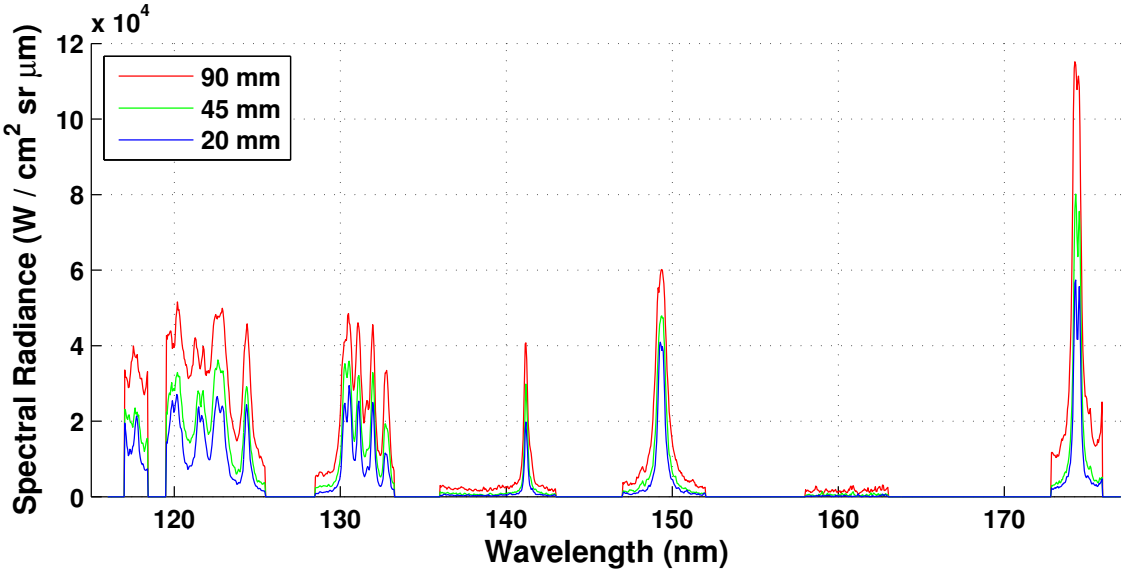


**Fig. 12 Comparison of spectra produced in the steady state emission region across models of lengths 90 mm, 45 mm and 20 mm at Condition 2.**

## V. Analysis

The finite spectral resolution of the spectroscopy system precludes the use of individual spectral lines in the investigation of the level of optical opacity of each transition through the shock layer. Simulations with an instrument function convolution were required to calculate a spectrum that accounted for the instrumental broadening of spectral lines. This was achieved using the CEA program [13] to calculate the equilibrium gas chemistry and Specair [5] to produce the emission spectrum. Specair is a radiation modelling and spectral line fitting program. It was the preferred program for this study due to the array of graphical features that can be used to aid in spectral line fitting.

The measured spectra were spatially averaged in the steady emission region of the shock layer and assumed to be at equilibrium. The equilibrium temperatures selected were 9,900 K and 12,400 K for Conditions 1 and 2 respectively based on best fits with the measured spectra and previous stagnation streamline measurements at these conditions [4]. Due to the high thermal sensitivity of the black-body limit in the VUV spectral range, this approach has been shown to obtain the temperature within an uncertainty of 2.0% and 2.5% for Conditions 1 and 2 respectively[4]. The radiating gas pressure for the simulations was set to the measured pitot pressure values for both conditions outlined in Table 1. Any contributions from the non-equilibrium edges of the shock layer were assumed to be negligible and therefore the gas thermochemistry was set to be constant for the entire line of sight. The computed and measured spectra for both conditions and each of the three model sizes are presented in Figure 13.

The equilibrium spectra computed showed good agreement with the measured values, suggesting the shock layer was in, or close to, thermochemical equilibrium in the steady emission region. A spectral line measured at 121 nm is not shown in the computed spectra and this is a result of hydrogen emission not being included in the Specair program. The measured and computed spectra were integrated across the regions outlined in Table 4. These regions were selected as they were void of contaminants. This approach allowed for the computation of the total radiance from a single, or discreet set of spectral lines, avoiding the complexities encountered due to spectral lines overlapping due to physical broadening mechanisms and spectral smearing due to the instrument

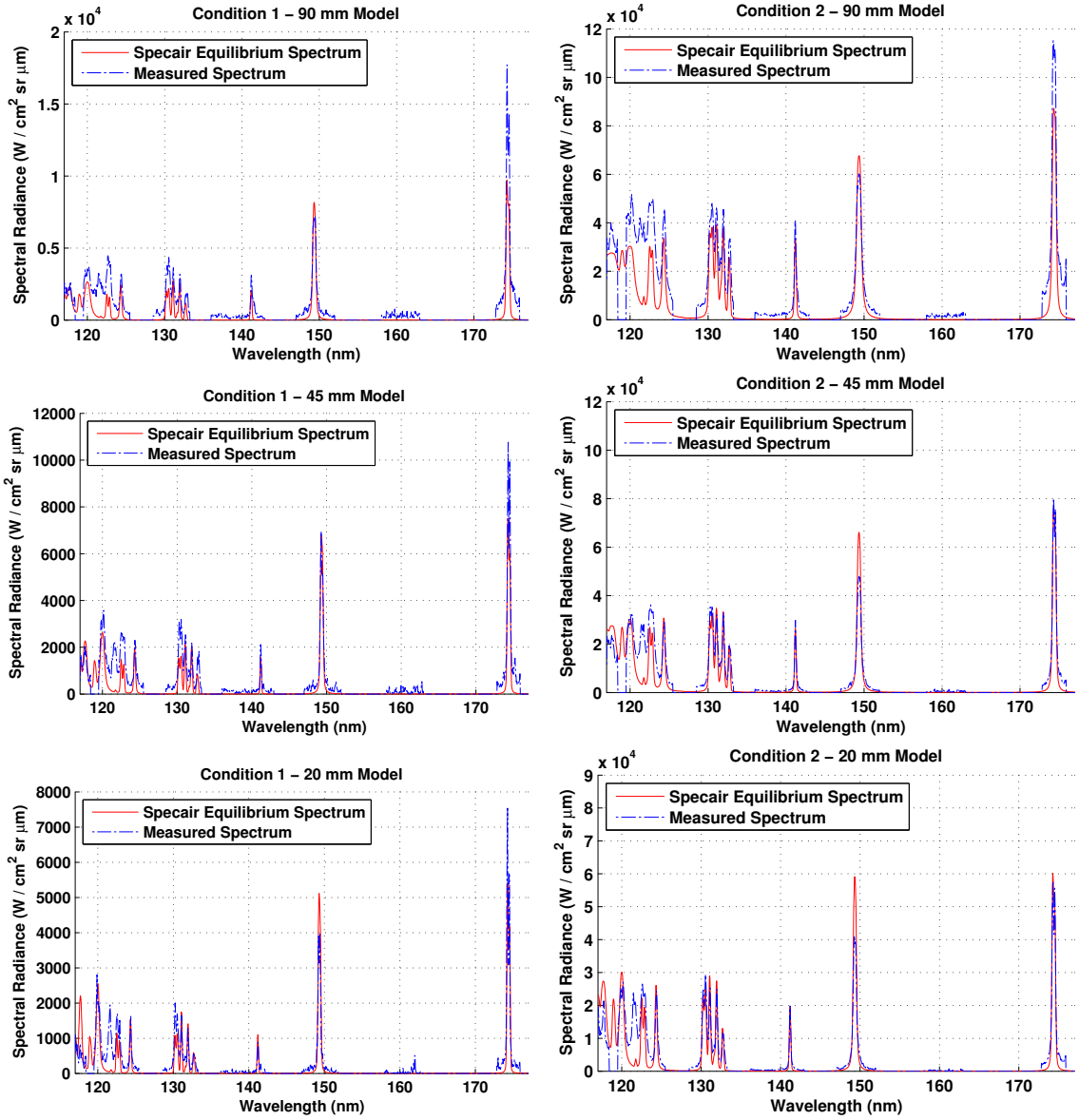


**Fig. 13 Comparisons of measured and computed spectra at equilibrium conditions. Condition 1 comparisons on the left hand side and Condition 2 comparisons on the right hand side. Model lengths: 90 mm - top, 45 mm - middle and 20 mm - bottom.**

function. Ratios of the integrated values were compared to remove any contributions from the non-equilibrium edges, assuming the edge effects remained constant between the different model sizes. The results of this analysis are presented in Figures 14 and 15. Region 3 at Condition 1 is omitted from the plot as a small aluminium peak contaminated the wings of the nitrogen spectral line. This aluminium peak was only observed at measurable levels for Condition 1. It was not observed in Condition 2 probably due to the higher equilibrium temperature resulting in a significantly higher

fraction of the aluminium becoming ionized.

**Table 4 Spectral regions used in integration analysis of optical thickness.**

| Region | Wavelength Range (nm) | Contributing Species |
|---|---|---|
| Region 1 | 124.0 - 125.0 | Nitrogen |
| Region 2 | 129.5 - 133.1 | Nitrogen and Oxygen |
| Region 3 | 140.8 - 141.6 | Nitrogen |
| Region 4 | 148.0 - 150.5 | Nitrogen |
| Region 5 | 173.5 - 175.3 | Nitrogen |

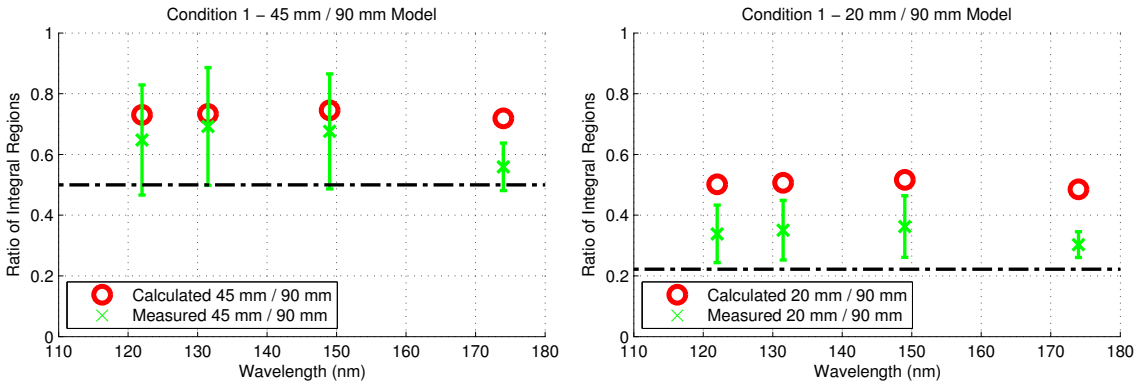


**Fig. 14 Computed and measured integrated region ratios for Condition 1. Integrated regions are outlined in Table 4. The dashed-dotted lines represent the ratios of model lengths.**

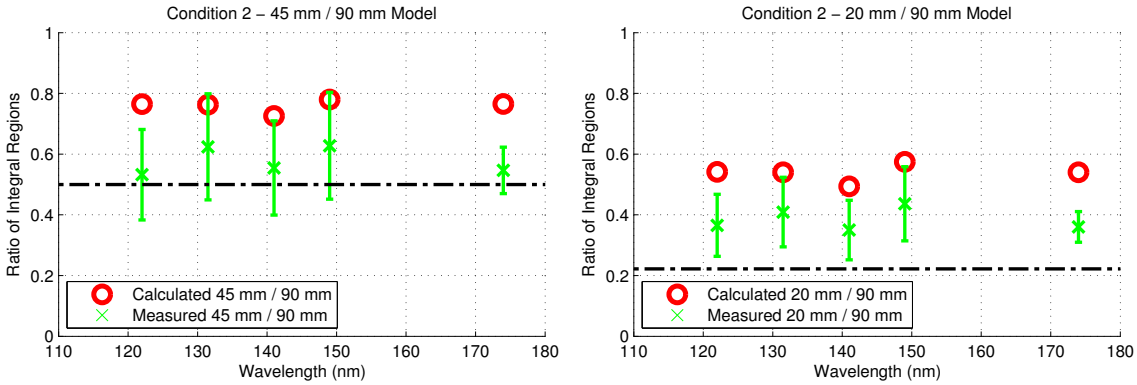


**Fig. 15 Computed and measured integrated region ratios for Condition 2. Integrated regions are outlined in Table 4. The dashed-dotted lines represent the ratios of model lengths.**

A previous repeatability study for this system found that spectral intensity measurements for these conditions, with a similar optical configuration, are repeatable to within 15% [4]. Based on

this uncertainty, the simulation results showed excellent agreement with measurements at Condition 1 between the 45 mm and 90 mm models. The simulated spectra over-predicted the measured self-absorption strength for the shorter 20 mm model at Condition 1. All calculated integral ratios at Condition 2 over-predict the measured values by a factor of approximately 1.3 across the entire spectral range. Having eliminated the possibility of this discrepancy being caused by the instrument function through the integration of spectral lines, possible explanations for this discrepancy are believed to be a combination of the non-equilibrium gas at either edge of the model, the three-dimensionality of the flow causing the shock front to curve around the model and the calculation of spectral line broadening. Three dimensional simulations are required to produce a line of sight thermochemical composition to account for the three-dimensionality and edge effects of the model in order to provide a more accurate comparison with measured spectral data.

### A. Computation of Optical Thickness

The simulated spectra provided good agreement with measurements and therefore the spectral modelling approach was considered to be valid. This modelling methodology was used to calculate spectral emission for the same gas assuming optical transparency, allowing for calculations of the optical thickness of the gas. Sample computed spectra for the 90 mm models are presented in Figures 16 and 17 on a logarithmic scale.

From Figures 16 and 17 it is apparent that the optically thin spectra predicts orders of magnitude higher spectral radiance compared with the optically opaque computations. Integrating across the wavelength bands outlined in Table 4 and comparing with experimental values obtained, it is possible to compute an optical opacity. Table 5 shows the percentage of radiation that is self-absorbed by the gas and provides an indicator of the optical thickness of the regions selected for this study. These percentages are based on the ratio of spectral emission using a simulated optically thin radiating gas and the experimentally measured radiating shock layer.

It is apparent that all spectral regions are highly optically opaque with at least 97.8% of the emitted radiation being absorbed before it can escape the shock layer. In particular, Regions 1 and 4 showed over 99.4% opacity for all three model sizes. Whilst these results show that the shock layer

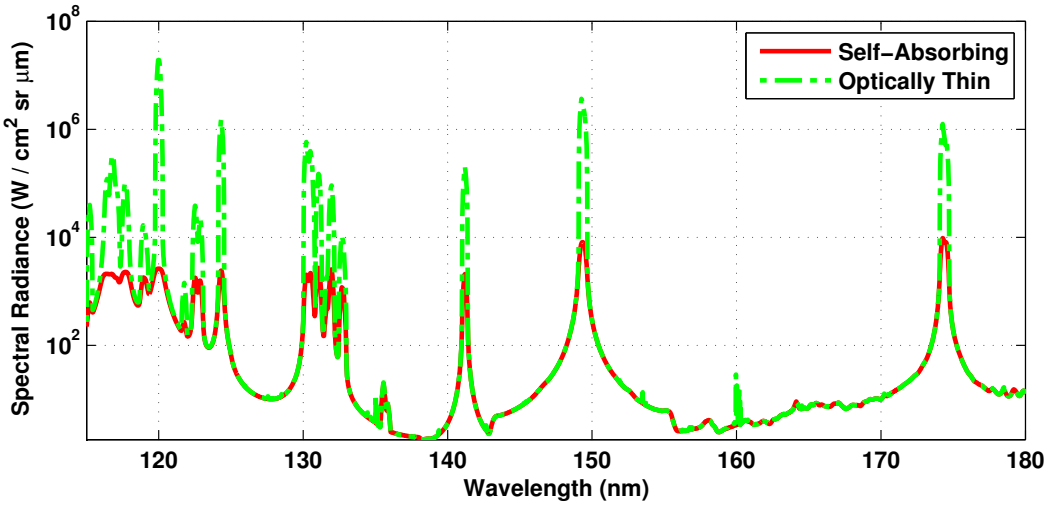


**Fig. 16 Comparison of the previously computed optically thick spectra, and emission from an optically thin gas for the 90 mm model at Condition 1.**

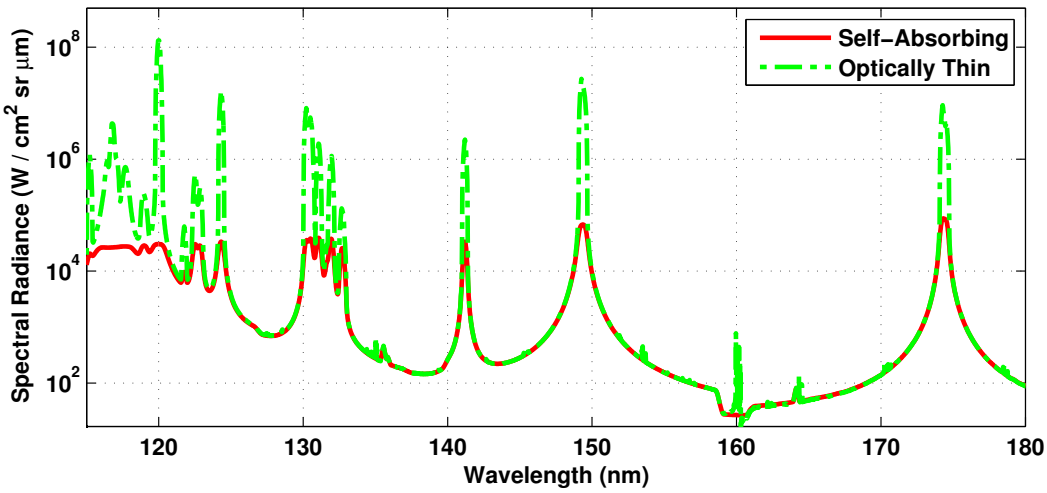


**Fig. 17 Comparison of the previously computed optically thick spectra, and emission from an optically thin gas for the 90 mm model at Condition 2.**

in all three models is highly optically opaque, there are significant increases in spectral radiance measured as the optical depth of the radiating flow field is increased, as summarised in Table 6 and Figure 18. This is due to the fact that the optical opacity is not changing significantly as the optical depth of radiating gas is increased. Consequently, almost the same small percentage of spectral radiance is transmitted through the bulk of the shock layer for the different size models, leading to the significant increases in total spectral radiance measured with increasing model length. As

**Table 5 Optical opacity percentage of integrated regions in the VUV spectral range calculated from simulated optically thin spectra and measured real gas spectra.**

| | Condition 1 | | | Condition 2 | | |
|---|---|---|---|---|---|---|
| Wavelength | 90 mm | 45 mm | 20 mm | 90 mm | 45 mm | 20 mm |
| Region 1 | 99.8% | 99.7% | 99.7% | 99.7% | 99.6% | 99.5% |
| Region 2 | 99.0% | 98.6% | 98.4% | 98.9% | 98.6% | 97.9% |
| Region 3 | N/A | N/A | N/A | 98.7% | 98.5% | 97.9% |
| Region 4 | 99.8% | 99.7% | 99.7% | 99.7% | 99.6% | 99.4% |
| Region 5 | 98.9% | 98.8% | 98.6% | 98.7% | 98.5% | 97.8% |
| Total | 99.5% | 99.4% | 99.3% | 99.4% | 99.2% | 98.9% |

the shock layers studied in these experiments are of comparable temperatures and particle number density to those observed in re-entry spacecraft, it can be concluded that shock standoff is strongly coupled to VUV radiative heat flux on a re-entry vehicle.

**Table 6 Experimentally measured total spectral radiance normalised to the 20 mm model.**

| | Condition 1 | | Condition 2 | |
|---|---|---|---|---|
| Spectral Radiance Normalised to 20 mm Model | 90 mm | 45 mm | 90 mm | 45 mm |
| Region 1 | 2.96 | 1.91 | 2.74 | 1.46 |
| Region 2 | 2.85 | 1.97 | 2.45 | 1.53 |
| Region 3 | N/A | N/A | 2.86 | 1.58 |
| Region 4 | 2.76 | 1.86 | 2.29 | 1.44 |
| Region 5 | 3.30 | 1.84 | 2.78 | 1.52 |
| Total | 3.00 | 1.89 | 2.55 | 1.50 |
| Normalised Length | 4.50 | 2.25 | 4.50 | 2.25 |

### B. Computational Spectra Without an Instrument Function

The computation of spectra for direct comparison with measurements was calculated using an instrument function convolution to account for the finite spectral resolution of the measurement system. Using the same approach but removing the convolution of the computed spectra with the instrument function, it is possible to provide a more detailed picture of the physical phenomena

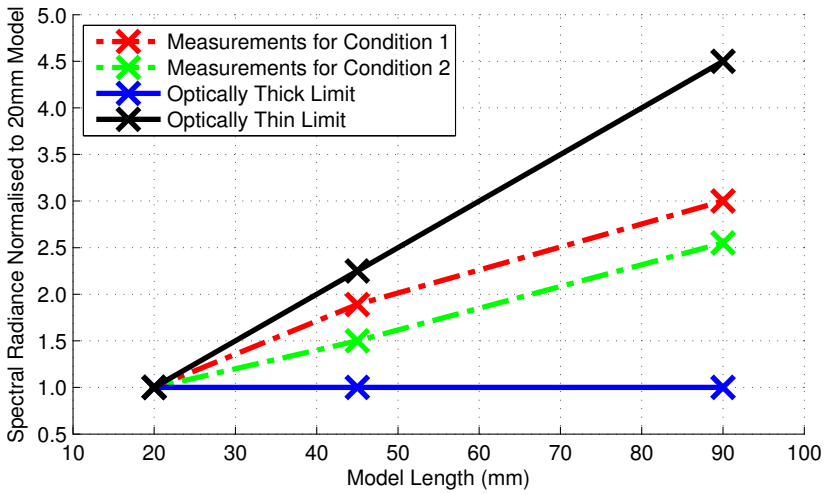


**Fig. 18 Measured increases in total VUV spectral radiance normalised to the 20 mm model with optically thick and thin limits superimposed.**

occurring in the radiating shock layer. Figures 19 and 20 present the spectra with the instrument function convolution removed.

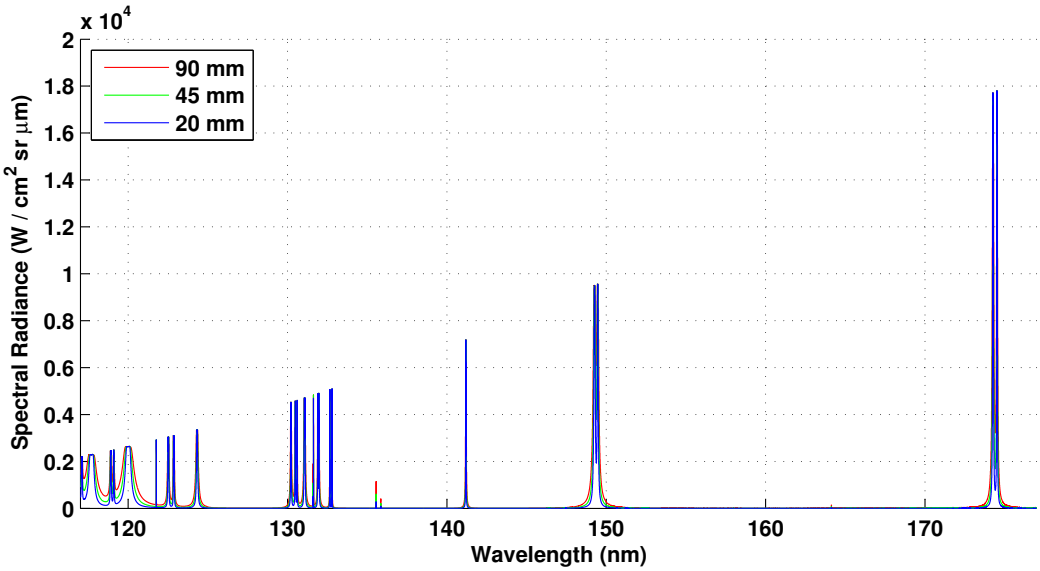


**Fig. 19 Computed spectra across models of lengths 90 mm, 45 mm and 20 mm at Condition 1 with no slit function convolution.**

It is immediately apparent that most spectral line peak intensities remain constant between the three depths of radiating flow fields, confirming the high opacity of the gas in the VUV spectral range. Furthermore, it can be concluded from the ratios of integral regions, which remain constant

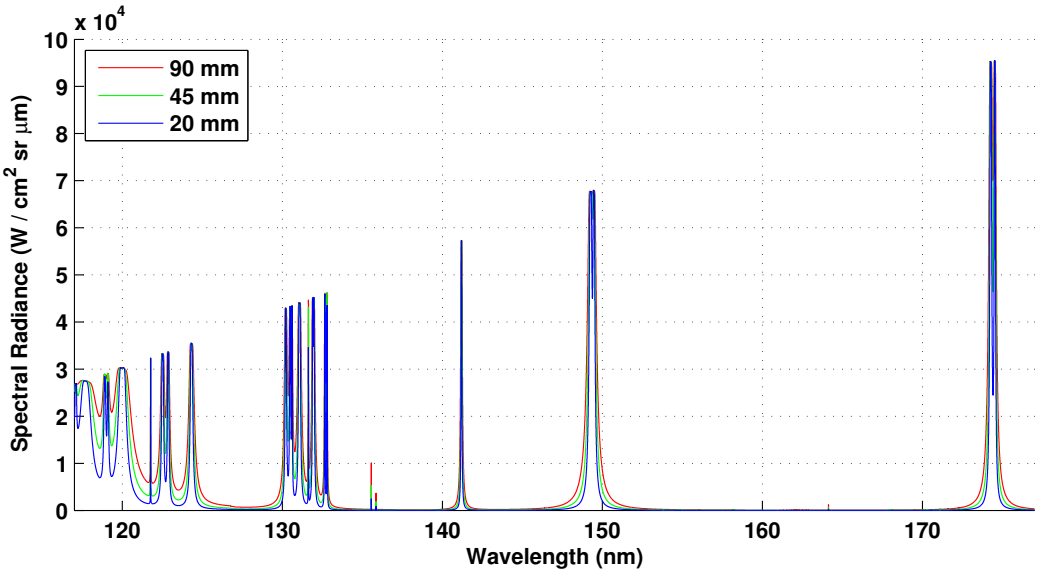


**Fig. 20 Computed spectra across models of lengths 90 mm, 45 mm and 20 mm at Condition 2 with no slit function convolution.**

with or without the instrument function convolution, that there are significant increases in spectral radiance from the wings of the spectral lines observed in the spectrum, even though the peak of the spectral line itself is not increasing in intensity. The physical broadening processes are so pronounced that most of the computed spectral lines overlap with neighbouring lines. This is highlighted by the spectral lines in the 129 nm to 133 nm and 147 nm to 151 nm regions presented in Figure 21.

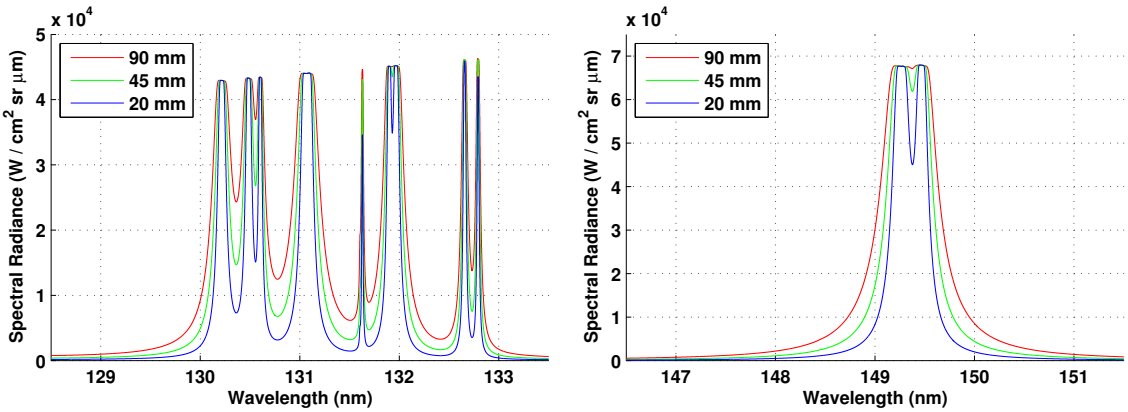


**Fig. 21 Computed spectra in two narrow spectral regions at Condition 2 without an instrument function convolution.**

## VI. Conclusions

This study has produced calibrated VUV emission spectral measurements across the surface of three different size models to investigate optical thickness and increases in radiation emission due to physical broadening mechanisms. Three models were used to allow for the creation of three depths of comparable radiating flow fields and spectral measurements were made between 115 nm and 180 nm, at two conditions representative of 10.0 km/s and 12.2 km/s flight equivalent velocities.

Spectra were computationally simulated using the CEA and Specair programs and good agreement was observed with measurements. Five spectral bands were selected for integration and analysis to overcome the complexities of spectral lines overlapping and the effect of the instrument function. Ratios of the integrated values were calculated for the different model lengths to eliminate the influence of the non-equilibrium edge effects, which were assumed to be constant for all models. The integral ratios provided an excellent match at Condition 1 between the 45 mm and 90 mm model measurements. For Condition 2, the computed ratios over-predicted the measured ratios by a factor of approximately 1.3 across the entire spectral range. This was attributed to a combination of the three-dimensionality of the flow field not being taken into account, the shot-to-shot repeatability of the system and the calculation of spectral line broadening in the simulations. It was concluded that three-dimensional simulations were required to accurately compute the thermochemisty through the entire line of sight for a more accurate comparison with measurements.

Simulations were carried out to calculate the total spectral emission that would be observed for an optically thin gas and compared with the measured values. This analysis concluded the shock layer was over 97.8% opaque for all the regions considered, and opacity values exceeded 99.4% for all measurements in Regions 1 and 4. Even at these high optical opacity levels, significant increases in spectral radiance were measured with increasing model length leading to the conclusion that the shock standoff is strongly coupled to VUV radiative heat flux on a re-entry vehicle.

Computational spectra without an instrument function convolution were produced to investigate the physical broadening occurring in the shock layer leading to the observed increases in integrated spectral radiance, and to decouple the instrument function from physical broadening mechanisms. This analysis concluded that the experimentally observed increases in spectral peak heights were

due to the instrument function and there were no increases in spectral line intensities at the nominal transition wavelength with increasing depths of radiating flow field. It is concluded from this study that the significant increases in spectral radiance measured with increasing depth of radiating flow field are due solely to physical broadening mechanisms and not through increases in spectral emission at the nominal wavelength of each transition. These results highlight the importance of accurately accounting for physical broadening mechanisms when computing the radiative heat flux in the VUV spectral range.

**Acknowledgements**

This work was supported by the Australian Post-graduate Award, Ablative Thermal Protective Systems grant from the Australian Research Council and Ablation Radiation Coupling grant from the European Space Agency. The authors would like to thank the workshop staff, operators of the X2 expansion tube facility and Christophe Laux for access to the Specair program.

**References**

[1] Kleb, B. and Johnston, C., "Uncertainty Analysis of Air Radiation for Lunar Return Shock Layers," *AIAA Atmospheric Flight Mechanics Conference and Exhibit*, AIAA, Honolulu Hawaii, 2008.

[2] Bose, D., McCorkle, E., Thompson, C., and Grinstead, J., "Analysis and Model Validation of Shock Layer Radiation in Air," *46th AIAA Aerospace Sciences Meeting and Exhibit*, AIAA, Reno, Nevada, 2008.

[3] Laux, C. O., Spence, T. G., Kruger, C. H., and Zare, R. N., "Optical diagnostics of atmospheric pressure air plasmas," *Plasma Sources Sci. Technol.*, 12:125-138, 2003

[4] Sheikh, U. A., Morgan, R. G., and McIntyre, T. J., "Vacuum Ultraviolet Spectral Measurements for Superorbital Earth Entry in the X2 Expansion Tube," *AIAA Journal*, 1-14, 10.2514/1.J054027, 2015.

[5] Laux, C. O., *Optical Diagnostics and Radiative Emission of Air Plasmas*, Ph.D. thesis, Stanford University, Stanford, CA, 1993.

[6] Auweter-Kurtz, M. and Wegmann, T., "Overview of IRS plasma wind tunnel facilities," Technical Report, DTIC Document, 2000.

[7] Sharma, S. P. and Park, C., "Operating charateristics of a 60-and 10-cm electric arc-driven shock tube, I-The driver. II-The driven section," *Journal of thermophysics and heat transfer*, Vol. 4, No. 3, 1990, pp. 259-265.

[8] Itoh, K., Ueda, S., Tanno, H., Komuro, T., and Sato, K., "Hypersonic aerothermodynamic and scramjet research using high enthalpy shock tunnel," *Shock Waves*, Vol. 12, No. 2, 2002, pp. 93-98.

[9] Sheikh, U. A., *Re-Entry Radiation Aerothermodynamics in the Vacuum Ultraviolet*, Ph.D. thesis, School of Mechanical and Mining Engineering, The University of Queensland, 2014.

[10] Gildfind, D., Morgan, R., McGilvray, M., Jacobs, P., Stalker, R., and Eichmann, T., "Free-piston driver optimisation for simulation of high Mach number scramjet flow conditions," *Shock Waves*, Vol. 21, No. 6, pp. 559–572, 2011

[11] Gildfind, D. E., *Development of High Total Pressure Scramjet Flow Conditions using the X2 Expansion Tube*, Ph.D. thesis, School of Mechanical and Mining Engineering, The University of Queensland, 2012.

[12] James, C., Gildfind, D. E., Morgan, R. G., Jacobs, P. A., and Zander, F., "Designing and Simulating High Enthalpy Expansion Tube Conditions," *2013 Asia-Pacific International Symposium on Aerospace Technology*, Sunport Hall, Takamatsu, Japan, 2013.

[13] McBride, B. J. and Gordon, S., "Computer program for calculating and fitting thermodynamic functions," Technical report, NASA Technical Report, RP-1271, 1992.

[14] Lu, H. C., Chen, K. K., Chen, H. F., Cheng, B. M., and Ogilvie, J. F., "Absorption cross section of molecular oxygen in the transition E3u-v=0 - X3g -v =0 at 38 K," *Astronomy and Astrophysics*, Vol. 520, 2010, pp. A19.

[15] Physikalisch-Technische-Bundesanstalt, "Calibration Certificate," 2011.

[16] Brandis, A., "Experimental study and modelling of non-equilibrium radiation during Titan and Martian entry," Ph.D. thesis, School of Mechanical and Mining Engineering, The University of Queensland, 2009.

[17] Ralchenko, Y., Jou, F. C., Kelleher, D. E., Kramida, A. E., Musgrove, A., Reader, J., Wiese, W. L., and Olsen, K., "NIST atomic spectra database (version 4.0)," National Institute of Standards and Technology, Gaithersburg, MD, 2010.